Lagrangian Coherent Structures and Turbulence Detection near the Hong Kong International Airport based on LIDAR Measurements

Wenbo Tang*

School of Mathematical and Statistical Sciences, Arizona State University, Tempe, AZ 85287

George Haller

Department of Mechanical Engineering, Massachusetts Institute of Technology, Cambridge, MA 02139

Pak Wai Chan

Hong Kong Observatory, Hong Kong, China

*E-mail: Wenbo.Tang@asu.edu

ABSTRACT

Terrain-disrupted turbulent airflow creates windshear to aircraft at the Hong Kong International Airport (HKIA). Better knowledge of the structures of the turbulent airflow will aid detection of the windshear and understanding of its impact on aircraft. A methodology is developed here to identify Lagrangian coherent structures (LCS) from the turbulent airflow sampled by Doppler velocity measurements of LIght Detection And Ranging (LIDAR) systems at HKIA. As a demonstration of this methodology, strong southerly flow associated with a tropical cyclone in April 2008 is analyzed. In this methodology, a variational method is first applied to the conical scans of the radial velocity from the LIDAR to derive the 2D wind field. Lagrangian airflow analysis is then used to identify the LCS in the airflow as revealed in the 2D wind data. The Lagrangian flow field is integrated in backward and forward time to locate updraft and downdraft in the flow, respectively. The results are compared with the vertical scans of the LIDAR which have not been used in the Lagrangian flow analysis. It is found that the updraft and downdraft identified from the Lagrangian flow analysis of the LIDAR conical scans are generally consistent with the airflow convergence and divergence as analyzed from the LIDAR vertical scans. The 2D Lagrangian flow analysis presented in the study, therefore, provides a way to infer the vertical air motion from the conical scan data of the LIDAR. This finding may lead to significant progress in LIDAR-based windshear detection, because the vertical wind shear component so far could not be measured directly by LIDAR or other ground-based weather sensors.

1. Introduction

Few major airports in the world display the same level of complexity in terrain feature as the Hong Kong International Airport (HKIA). Situated in the vicinity of the Lantau Island with mountain peaks up to almost 1 km AMSL and valleys of only around 400 m AMSL in between, HKIA is exposed to complicated and ever-changing flow structures generated off the peaks and valleys of its mountainous neighborhood under various weather conditions. In order to monitor these complex wind flows in real time, two Doppler LIght Detecting And Ranging (LIDAR) systems are implemented at HKIA. As a result, line-of-sight (LOS) velocities of the wind vectors are regularly available.

Variational wind retrieval techniques have been applied to estimate the two-dimensional wind fields based on conical scans at small elevation angles (Chan and Shao 2007). Discussions on the two-dimensional turbulent structure of real time terminal winds are primarily based on this retrieved wind data. Coherent structures near the airport — such as vortices, mountain wakes, divergences and convergences — have been identified by visually inspecting streamlines generated from the retrieved wind vectors.

While large-scale structures can be revealed by staring at individual instantaneous velocity plots, small-scale events are harder to detect. The procedure, inefficient at best, could also be misleading: instantaneous streamline sketches of an unsteady flow do not give an objective characterization of actually particle motion in the air.

Recently, a frame-independent extraction of Lagrangian Coherent Structures (LCS) in turbulent flows through Lyapunov exponents has been developed (Haller 2001). This method has been implemented to analyze geophysical flow structures by objective feature extraction from two- and three-dimensional velocity fields (Lekien et al. 2005; Coulliette et al. 2007; Tang et al. 2009). The method operates in the Lagrangian frame and analyzes the relative motion of fluid particles. The LCS turn out to be distinguished sets of fluid particles that attract or repel other particles at locally the highest rate in the flow. In our present context, the LCS marking the most unstable atmospheric motions pose threat to flight safety: airplanes will experience the strongest disturbance when flying through such structures.

In this paper, we develop an LCS extraction method for the two-dimensional wind retrieval data at HKIA, from which we will also infer the three-dimensional structure of the flow. Due to limited data coverage for the purposes of Lagrangian analysis, we introduce a technique that allows trajectory simulation outside the retrieval domain without the introduction of spurious structures.

We test the above method on a strong southerly flow associated with a tropical cyclone in April 2008. In this case, PPI scans at two elevation angles are used to generate the two-dimensional retrieved wind fields. LCS analysis is then performed by integrating fluid particle trajectories in forward- and backward-time using the wind fields, and computing Direct Lyapunov Exponents (DLE) based on these trajectories. The DLE fields are also compared with vertical slice scans at two azimuthal angles along the runway corridor and into a mountain gap to confirm our interpretation of the LCS.

Techniques for wind retrieval of the three-dimensional velocity data have also been developed for some time (Sun et al. 1991; Qiu and Xu 1992). It appears that LCS extracted from the full three-dimensional flow field reveals more information. In our study of the flow near HKIA, however, we are limited by the number of PPI angles and the need for fast retrieval of real-time flow structures. For this reason, only two-dimensional data are considered in this study.

2. The remotely sensed data and wind retrieval

For wind monitoring at HKIA, two coherent Doppler LIDARs are operated by the Hong Kong Observatory (HKO). Each LIDAR operates at a wavelength of 2 microns with pulse energy of about 2 mJ. The pulse repetition frequency is 500 Hz and line-of-sight data are output at 10 Hz (i.e. an average of 50 pulses for each datum). With a range resolution of about 100 m and 1,024 range bins, the measurement distance starts from about 400 m and is up to 10 km. The maximum unambiguous velocity is normally 20 m/s, extendable to 40 m/s at the expense of the range.

In order to reveal the most important coherent structures impacting flights, the LIDAR systems at HKIA have employed a special scan strategy, comprising the following scans:

(a) Plan-position Indicator (PPI) scans (or conical scans) to provide the weather forecasters with an overview of the wind condition in the vicinity of HKIA - There are three PPI scans at different elevation angles. The PPI scans are blocked by the air traffic control tower to the north. Moreover, as a laser safety measure, sector blanking has been applied for the residential area outside HKIA.

(b) Range-height Indicator (RHI) scans (or vertical-slice scans) to measure the vertical structure of the windshear features, e.g. interaction between sea breeze and the background flow, hydraulic jump in cross-mountain airflow, etc.

(c) Glide-path scans to focus on the wind conditions along the glide paths for operational windshear alerting — The LIDAR estimates the headwind profile to be encountered by the aircraft and significant wind changes in the profile are detected automatically.

The 2-D wind retrieval algorithm for LIDAR is modified from a two-step variational method for radar (Qiu et al. 2006). The cost function J to be minimized is given by:

$$\begin{aligned} J(u,v) &= J_1 + J_2 + J_3 + J_4 + J_5 + J_6 \\ &= \sum_{i,j}\{W_1[(u-u_B)^2 + (v-v_B)^2] + W_2(v_r - v_r^{obs}) + W_3(\frac{\partial u}{\partial x} + \frac{\partial v}{\partial y})^2 \\ &+ W_4(\frac{\partial v}{\partial x} - \frac{\partial u}{\partial y})^2 + W_5(\nabla^2 u + \nabla^2 v)^2 + \sum_n [W_6(\frac{\partial v_r^{obs}}{\partial t} + u\frac{\partial v_r^{obs}}{\partial x} + v\frac{\partial v_r^{obs}}{\partial y})^2]\}. \quad (1) \end{aligned}$$

where u and v are the components of the retrieved wind field, subscript B the background field (generated from LIDAR radial velocity in the way described in Qiu et al. (2006)), v_r the retrieved radial velocity, superscript *obs* the observed values, i and j the horizontal grid point and n the time index (three consecutive scans are used in each analysis). The weights are: $W_1 = 0.1$ (after the first step retrieval), $W_2 = 1, W_3 = W_4 = W_5 = 0.1$ and $W_6 = 10^4$. They are chosen empirically in this paper to ensure that the constraints have proper orders of magnitude.

Before performing the retrieval, the radial velocity data are quality-controlled to remove the outliers due to, for instance, reflection from clutters. The main source of clutter is the moving aircraft in the sky and the clutter does not occur very frequently (in the order of a few per day). Such outliers could be detected by mimicking visual inspection to compare each piece of radial velocity with the data points around, and replaced by a median-filtered value if the difference between them is larger than a pre-defined threshold. The threshold is determined from the frequency distribution of velocity difference between adjacent range/azimuthal gates of the LIDAR over a long period of time. The quality-controlled radial velocity in the range-azimuth coordinate system is then interpolated to a Cartesian grid with resolution of 100 m using Barnes scheme.

Figure 1a shows a typical LIDAR output. The color map indicates the LOS velocity, with positive values denoting motion away and negative values denoting motion towards the LIDAR. Sector blanking and tower blockage are apparent in this figure. Also note that the LIDAR is scanning at 1.4 degrees, the light beams cannot penetrate the mountains, hence there is poor data coverage South of the airport. The white contours indicate constant elevation of the terrain near the airport at 100 m intervals. The two runways are also shown as rectangular stripes, with runway corridors marked at the ends of the runways with tick marks at 1, 2 and 3 nautical miles away from the runway ends. Figure 1b shows streamlines and wind vectors generated from the retrieved wind field. Wind velocities in the blocked regions are obtained with the retrieval technique. These data can be treated roughly as horizontal wind velocity near the surface of the terrain. From reading these figures, one can only infer a few streak features originating from the terrain indicated by the white ellipses in the figure. Clearly finer flow structures are not easy to identify either from the LOS velocity map or from the streamlines.

3. Flow topology and interpretations

A frame-independent measure of instability in an arbitrary fluid flow is the Direct Lyapunov Exponent (DLE). Specifically, let $\mathbf{v}(\mathbf{x}, t)$ denote the velocity field associated with the retrieved two-dimensional terminal flow, we can integrate the equation

$$\dot{\mathbf{x}}(t) = \mathbf{v}(\mathbf{x}(t), t), \qquad \mathbf{x}(t_0) = \mathbf{x_0}, \tag{2}$$

to obtain the fluid particle trajectory $\mathbf{x}(t)$ originating from position $\mathbf{x}_0$ at time t_0. The position $\mathbf{x}(t;\mathbf{x}_0,t_0)$ on a trajectory is a map of its initial condition $\mathbf{x}_0$ at time t.

Using this flow map, we define the Cauchy-Green strain tensor and the DLE field as

$$\mathbf{M}_{t_0}^{t}(\mathbf{x}_0) \equiv \left[\frac{\partial \mathbf{x}(t;\mathbf{x}_0,t_0)}{\partial \mathbf{x}_0}\right]^T \left[\frac{\partial \mathbf{x}(t;\mathbf{x}_0,t_0)}{\partial \mathbf{x_0}}\right], \qquad DLE_{t_0}^{t}(\mathbf{x}_0) \equiv \frac{1}{2\,(t-t_0)} \log \lambda_{\max}(M)\,,$$

where $[\partial \mathbf{x}/\partial \mathbf{x}_0]^T$ denotes the transpose of the deformation gradient tensor $\partial \mathbf{x}/\partial \mathbf{x}_0$ and $\lambda_{\max}(M)$ denotes the maximum eigenvalue of M. Effectively, the DLE field is a scalar field that associates with each initial position $\mathbf{x_0}$ the maximal rate of stretching along its trajectory $\mathbf{x}(t;\mathbf{x}_0,t_0)$. Fluid particle trajectories are obtained by integrating Eq. (2). When computed from forward-(backward-)time trajectories, the DLE field measures the largest separation (contraction) of nearby trajectories, and so local maximizers of DLE denote repelling (attracting) structures.

Special attention has been paid in this study to the fact that we are analyzing a data set on a spatially limited domain. The observational radius of the LIDARs is 10 km. During retrieval, velocity domain is reduced to a square of length 15 km. For a typical wind velocity of 20 m/s, on average fluid trajectories dwell in the square domain for 750 seconds. Velocity information outside this domain is unknown and trajectories in similar analyses have traditionally been stopped at the boundaries. As a result, the boundaries become artificial attractors and integration time is limited to a time scale much less than the dwelling time (so at least some trajectories are still in the domain and unaffected by the artificial attractors). However, DLE is effective at revealing LCS only when integration time is long enough for the attractors/repellers to become distinguishable from other trajectories (Haller 2001).

To address the above challenge, we use a linear best fit to obtain a smoothly connecting, divergence-free external flow and continue fluid trajectories outside the original domain. With the implementation of this extrapolation, we fully exploit the nonlinearity of the flow *inside* the domain, without introducing additional nonlinearity (as stopping trajectories at boundaries does) to the flow.

Note that the two-dimensional wind field is obtained from small elevation angle PPI scans, discussions of LCS can be interpreted as the near ground portion of three-dimensional structures. For example, repelling LCS could arise from horizontal divergence of trajectories (voids are filled by trajectories from behind) or vertical supply of trajectories (voids are filled by trajectories from above). The first corresponds to diverging horizontal windshear and the latter corresponds to downdrafts. Likewise, attracting LCS corresponds to converging windshear and updrafts. Assuming that the three-dimensional atmospheric flow is divergence free, one can integrate the instantaneous horizontal divergence

$$DIV_{t_0}^{t}(\mathbf{x}_0) = \int_{t_0}^{t} \left[\frac{\partial u(\mathbf{x})}{\partial x} + \frac{\partial v(\mathbf{x})}{\partial y} \right] \mathrm{d}t \tag{3}$$

along a trajectory $\mathbf{x}(t; \mathbf{x}_0, t_0)$ to infer vertical motion and compare with the DLE fields. $DIV_{t_0}^{t}(\mathbf{x}_0)$ is referred to as the Lagrangian divergence. If air flow is purely horizontal, Lagrangian divergence will be zero yet we still see maximizers of the DLE fields. They correspond to changes of horizontal directions of fluid particle trajectories. On the other hand, if there is consistent vertical motion, downdrafts (updrafts) will consistently repel (attract) nearby trajectories, hence its horizontal divergence is consistently positive (negative). As such, local maximizers of forward-(backward-)time DLE associated with local maximizers of Lagrangian divergence (convergence) corresponds to downdrafts (updrafts), whereas local maximizers of DLE without such correlation indicate horizontal windshear. In order to test the accuracy of these criteria, we compare the extracted LCS with vertical RHI scans, which are not used in the horizontal wind retrieval, to interpret the flow structures and their evolution near the airport.

4. Case Study

We focus our analyses on a southerly flow case on April 19th, 2008. After a rain band associated with a tropical cyclone, there is good data coverage from 1330UTC to 2000UTC, giving us a reasonable window to analyze the evolution of flow structures. PPI scans at elevation angles of 1.4 and 3 degrees are available at roughly 150 second intervals. To perform Lagrangian analyses we need to integrate fluid trajectories inside the domain. As indicated earlier, sector blanking and tower and mountain blockages leave poor coverage of LIDAR data in certain regions within the domain. As a result, retrieved velocity in these blank areas reflect most erroneous data persistent at all times. To allow trajectories to be advected by the true airflow more we choose to use the data from the LIDAR next to the northern runway (113.92°E, 22.313°N) as it is further away from the mountains.

Figure 2 shows the forward- and backward-time DLE computed from the retrieved wind velocity at PPI angle 1.4°, along with the Lagrangian divergence at 142901UTC on April 19th, 2008. Since the average residence time of trajectories in the domain is about 750 seconds, we choose this as the integration time for trajectories. Therefore, effectively Fig. 2 contains 6 frames of LIDAR data (it's hard to increase the frequency of PPI scans as the LIDAR needs to perform other scanning strategies). Note that the time step in integration is chosen to be 3 seconds to ensure that trajectories move less than a grid box (100 m) in each time step. Cubic interpolation is used in both space and time for high accuracy of the trajectories.

The units of the color maps in Fig. 2 are s^{-1}. The most notable structures in Fig. 2 are the successive hairpin structures originating from the Southwest corner of the domain in Figs. 2b,d. These figures are the DLE and DIV fields computed in backward-time and so highlighters in these fields correspond to updrafts near ground. The external flow enters the domain from the Southwest corner. The hairpin structures correlate very well with several mountain peaks on Lantau Island. Three successive hairpin structures originated from a peak A (marked white in Fig. 2b) has been labeled A_1 through A_3, in the order that they were generated. Three more hairpin structures next to them (marked B_1 through B_3) seem to associate with flow passing peak B. The generation sites of these hairpin structures do not seem to be exactly on the mountain top, this may be due to inaccuracies of retrieved data in the mountain blocked regions. However, we do trust the existence of these flow structures as they get continuously advected into LIDAR observable domains as time progresses. Towards the right half of the domain in these two figures, several streak structures arise, similar to those outlined in Fig. 1b but with more clarity with the DLE field (labeled C).

We use Fig. 2d as an example to differentiate updrafts and horizontal convergence. There is in general good correlation between negative values of DIV and highlighters of DLE (note that the strongly red regions are *inside* the hairpins). It is not surprising that negative regions of the DIV field is not as pronounced as the DLE ridges. Once trajectories leave the retrieval domain they are allowed to diverge but their horizontal divergence is zero due to the extrapolation scheme we specify, hence the integrated Lagrangian divergence only reveals partial information over time. (For example, trajectories in the most pronounced ridge at the Southwest corner of Fig. 2b would leave the domain very quickly when integrating in backward time. The DLE field still reveals trajectory separation yet Lagrangian divergence is mostly 0 for the duration of integration, and thus DIV is not strongly negative for those trajectories.)

Figs. 2a,c are the DLE and DIV fields computed in forward-time and they highlight downdrafts. There is also good correlation between highlighters of the DLE field and positive values of DIV, while noting that the strongly negative divergence corresponds to those regions inside the DLE ridges. There seems to be less ridges in Fig. 2a as compared to Fig.2b. However we note that the standard deviation of DLE values in Fig. 2a is smaller than that in Fig. 2b, this effectively makes ridges less pronounced in this figure.

Indeed, 142901UTC is the time when a vertical RHI scan is performed at the 258° azimuth, along the runway corridor. We superimpose the RHI scan with DLE fields in Fig. 3 to discuss the vertical flow structures. In fact, vertical structures are better understood with the gradient of the LOS velocity. When velocity changes the fastest (largest gradient), we expect the flow to have strongest convergence/divergence, and so there is vertical motion associated with such structures. We adopt a coordinate such that the radial distance is negative away and increases as it approaches the LIDAR. In such a coordinate system, convergence (updraft) corresponds to maximum rate of increase in LOS velocity as one move towards the LIDAR, or LOS velocity gradient maximum. By the same token, divergence (downdraft) corresponds to LOS gradient minimum. We show comparison of the DLE fields with RHI scans in Fig. 3 to infer the vertical structures. The color maps in this figure show LOS velocity gradients. Maxima and minima in the maps indicate regions of largest instantaneous convergence and divergence of the airflow. We superimpose the interpolated

DLE fields generated with the 1.4°(red) and 3°(black) PPI scans. Fig. 3a shows forward-time DLE interpolated at the 258° azimuth, and Fig. 3b shows that for the backward-time DLE. Correlation in DLE peaks and the RHI gradient fields should be understood at the PPI scan angles, or the dashed lines. For example, the red dashed line in Fig. 3b shows the 1.4° PPI scanning angle. Along this line we observe several RHI velocity gradient maxima. The backward-time DLE peaks correlate well with these maxima as indicated by the upward pointing arrows, especially for those larger peaks. Correlation of the RHI scan with the other three DLE interpolations are understood in the same manner. Therefore, we can in general assume downdrafts associated with ridges in Fig. 2a and updrafts associated with ridges in Fig. 2b and infer the flow structure.

From the information at hand we infer the three dimensional flow structures to be series of hairpin structures originated from the peaks at the Southwest corner of the domain. These structures undergo the following series of evolution: flow separate from the mountain peak and reattach to form bubble → bubble grows and its ends are advected downstream to form the two prongs of the hairpin → bubble saturates and detach from the peak, advected downstream → new bubbles form at the peak. Such an evolution is illustrated in Fig. 4, for the attracting structures, or updrafts. The time interval for different plots are at 4 minutes, and Fig. 4d is at 1429UTC, when an RHI scan at 258° azimuth is available (analyzed in Fig. 5). Individual hairpin vortices, in the order that they appear, are labeled A_1 through A_3 and their evolution is revealed in Fig. 4. From the series of plots we see the evolution of the attracting structures and their detachment from the mountain peak. As they are advected outside of the domain, they give way to the generation of new hairpin structures. Clearly what we observe from the LCS is terrain induced flow structure generated at mountain peaks on Lantau Island. These structures would not be obtained if one tries to read directly from those plots in Fig. 1. It is worth noting that similar structures of successive bubble generation and detachment have been observed in a different tropical cyclone case in Hong Kong using Terminal Doppler Weather Radar (TDWR) (Shun et al. 2003), ascertaining the typical flow structure arise in like flow conditions.

With the aid of the RHI scan, we finally illustrate the hairpin vortex A_2 at 1429UTC in Fig. 5. Fig. 5a shows the LOS velocity return based on the RHI scan. Two patches of LOS anomalies are outlined with the dashed ellipses. From them we estimate the vertical length scale of near ground structures to be about 250 m. In Fig. 5b we show the inferred structures. Backward-time DLE is used to represent horizontal slice of the flow structure and the radial gradient of RHI scan is used to represent vertical slice of the flow structure. First, we see good correlation between the DLE ridges in the conical scan and maxima of gradient in the RHI scan. As explained earlier, trajectories converge from both sides of these maxima, which confirms the interpretation that backward-time DLE correlate with updrafts. We also expect downdraft between the two updrafts, as inferred by the minimum in the gradient of the RHI scan. Correlation of this minimum with forward-time DLE is also observed from the data (c.f. the middle red arrow and a correlating forward-time DLE peak in Fig. 3a). With this information we can outline the hairpin vortex structure. As updrafts ascend, at roughly 250 m they will turn around and start to descend. This forms two counter rotation vortices as projected on the RHI scan in Fig. 5b. We also plot several trajectories at the head of the hairpin so the overall structure is apparent. The dashed lines show boundaries of the flow structure and the merging center which forms the downdraft. We omit comparison with the RHI scan at 163° azimuth, as it points into the mountain gap, which is in an area of poor data coverage. Also the scan is pointed higher (with elevation angles 3.6° and above), making the comparison less meaningful away from the LIDAR.

5. Conclusions

In this study we have developed an algorithm to extract LCS from two-dimensional wind data retrieved from LIDAR measurements. By introducing an extrapolation scheme for global flow information, we have extended Lagrangian trajectory integration beyond the observational domain and fully exploited the nonlinearity in the retrieved data sets. We have established a criterion in differentiating the types of coherent structures to identify updrafts, downdrafts and horizontal windshear.

For the tropical cyclone case analyzed, based on the near-ground behavior of fluid trajectories, we have identified the consecutive generation, detachment, advection and regeneration of hairpin vortices from a mountain peak near the airport, along with other structures advected into the domain with the external flow. The extracted coherent structures correlate well with the vertical structures obtained from RHI scans at the two azimuthal angles. Note that since RHI scans are only available at a few azimuthal angles, the LCS provides a complete picture of the near ground vertical and horizontal structure of the flow. Similar flow structures has been observed with TDWR velocity estimates from another tropical cyclone case near HKIA, ascertaining the flow structures we infer from this case.

Crucial advantages of using LCS to identify turbulence structures are frame independence and clarity. As the LCS are purely describing relative motion of nearby trajectories, they are not affected by the choice of frame, whereas the usual quantities in Eulerian frame such as velocity or vorticity are not invariant quantities subject to arbitrary translation of the observational frames and could lead to inaccurate description of flow structures. Additionally, LCS reveal structures in more detail than Eulerian descriptions. This is apparent when comparing Fig. 2 to Fig. 1. With stronger contrast with their ambient, one can accurately interpret the boundaries of flow structures near the airport. As such, it is beneficial to perform wind retrieval and LCS extraction based on TDWR data as those discussed in Shun et al. (2003) in the same manner to ascertain the relationship between the observed Strouhal numbers and the LCS characteristics.

For LCS extraction in real time, only the attracting structures and converging horizontal windshear can be detected from the observational data. This is because attracting structure and converging windshear are obtained from backward integration starting from the present time over available past data. By contrast, to locate repelling structures, we would need to advect trajectories in forward-time into the future, using velocity data that is not yet available from the LIDAR scan. Consequently, real-time extraction of repelling structures and diverging windshear is not feasible. As a workaround, one could run a sub-mesoscale simulation initiated from LIDAR measurements to constantly forecast the velocity field 15 minutes ahead, and use the forecast data to integrate trajectories into the future.

One constraint on the accuracy of LCS is the azimuthal velocity. As pointed out by Chan and Shao (2007), their variational technique yields highly accurate radial velocity, but there is huge uncertainty in the azimuth. Since it is not directly obtained from the LIDAR, we are relying heavily on various assumption in the retrieval technique. When integrating the flow to obtain trajectories, both radial and azimuthal velocities are of equal weight, and so uncertainties in the azimuthal velocities strongly affect the final result of the LCS. Therefore, it is meaningful to conduct statistical analyses on the retrieved two-dimensional wind data to address the uncertainties of the LCS.

We also realize that for operational use of LCS to aid flight control, we would need a better understanding of the correlation between LCS and existing flight data. By matching flight data with extracted flow structures, we can identify the types of LCS that have the most significant impact on take-off and landing. The results of such an analysis will appear elsewhere.

REFERENCES

Chan, P. W. and A. M. Shao, 2007: Depiction of complex airflow near hong kong international airport using a doppler lidar with a two-dimensional wind retrieval technique. *Meteorol. Z.*, **16, No. 5**, 491–504.

Coulliette, C., F. Lekien, J. D. Paduano, G. Haller, and J. E. Marsden, 2007: Optimal pollution mitigation in monterey bay based on coastal radar data and nonlinear dynamics. *Environ. Sci. Technol.*, **41**, 6562–6572.

Haller, G., 2001: Distinguished material surfaces and coherent structures in three-dimensional fluid flows. *Physica D*, **149**, 248–277.

Lekien, F., C. Coulliette, A. J. Mariano, E. H. Ryan, L. K. Shay, G. Haller, and J. E. Marsden, 2005: Pollution release tied to invariant manifolds: A case study for the coast of florida. *Physica D*, **210**, 1–20.

Qiu, C. J., A. M. Shao, S. Liu, and Q. Xu, 2006: A two-step variational method for three-dimensional wind retrieval from single doppler radar. *Meteorol. Atmos. Phys.*, **91**, 1–8.

Qiu, C. J. and Q. Xu, 1992: A simple adjoint method of wind analysis for single-doppler data. *J. Atmos. Oceanic Technol.*, **9**, 588–598.

Shun, C. M., S. Y. Lau, and O. S. M. Lee, 2003: Terminal doppler weather radar observation of atmospheric flow over complex terrain during tropical cyclone passages. *J. Applied Meteorol.*, **42**, 1697–1710.

Sun, J., D. Flicker, and D. Lilly, 1991: Recovery of three dimensional wind and temperature fields from simulated doppler radar data. *J. Atmos. Sci.*, **48**, 876–890.

Tang, W., M. Mathur, G. Haller, D. C. Hahn, and F. H. Ruggiero, 2009: Lagrangian coherent structures near a subtropical jet stream. *J. Atmos. Sci. submitted*.

List of Figures

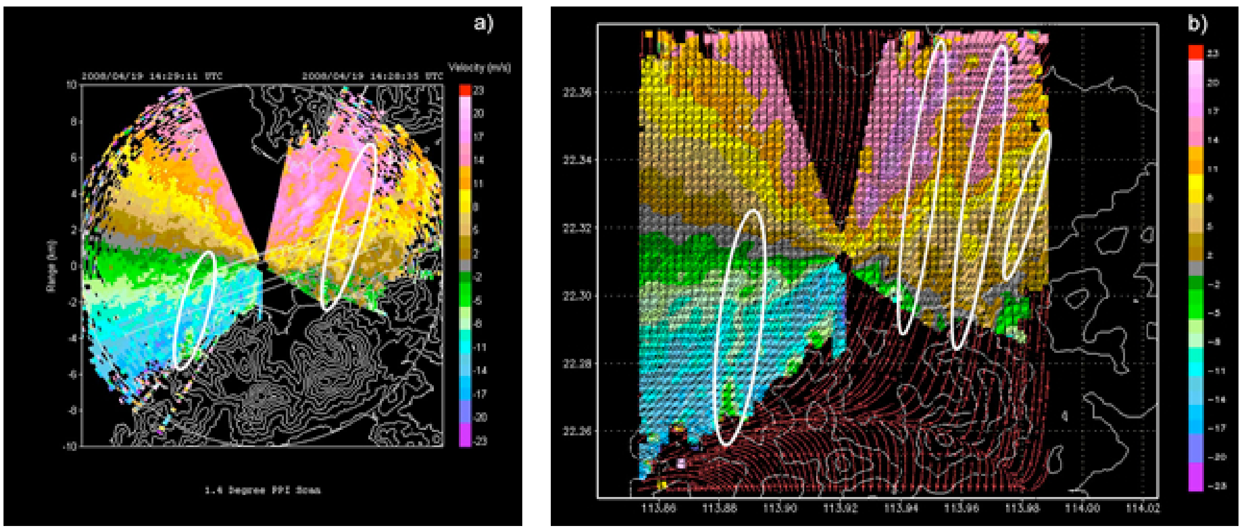

FIG. 1. a) Line-Of-Sight velocity measured by the Northern LIDAR at 142911UTC. Posivite values indicate LOS velocity away from LIDAR. White contours show the mountainous topography next to HKIA at 100m intervals. The two runways and runway corridors are also shown in the center of the figure. b) Wind vectors and streamlines based on the retrieved velocity at the same time. Only a few streak features can be inferred from the LOS velocity and streamline plot in the LIDAR covered regions. They are highlighted in both figures as white ellipses.

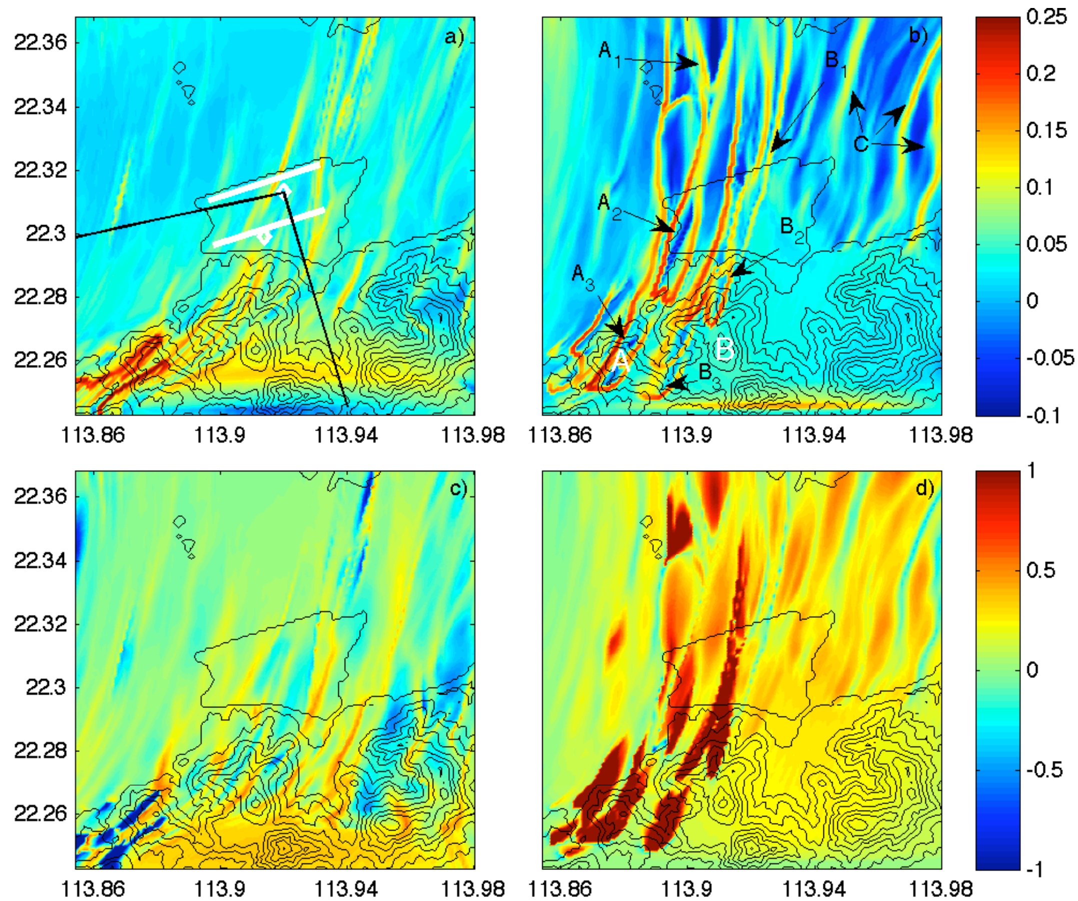

Fig. 2. Lagrangian Coherent Structures obtained from the two-dimensional wind retrieval. a) Forward-time DLE field. Maximizers indicate repelling structures. Also shown are the two runways (white stripes), LIDARs (white diamonds) and directions of the RHI scans at 258° (black solid line aligned with the runways) and 163° (black solid line transverse to the Southern runway). b) Backward-time DLE field. Maximizers indicate attracting structures. Hairpin structures associated with two mountain peaks A and B are labeled A_1 through A_3 and B_1 through B_3 accordingly. Several streak features are labeled C. c) Forward-time Lagrangian divergence. d) Backward-time Lagrangian divergence. For both c) and d), positive (negative) values indicate downward (upward) motion near ground over the time of integration.

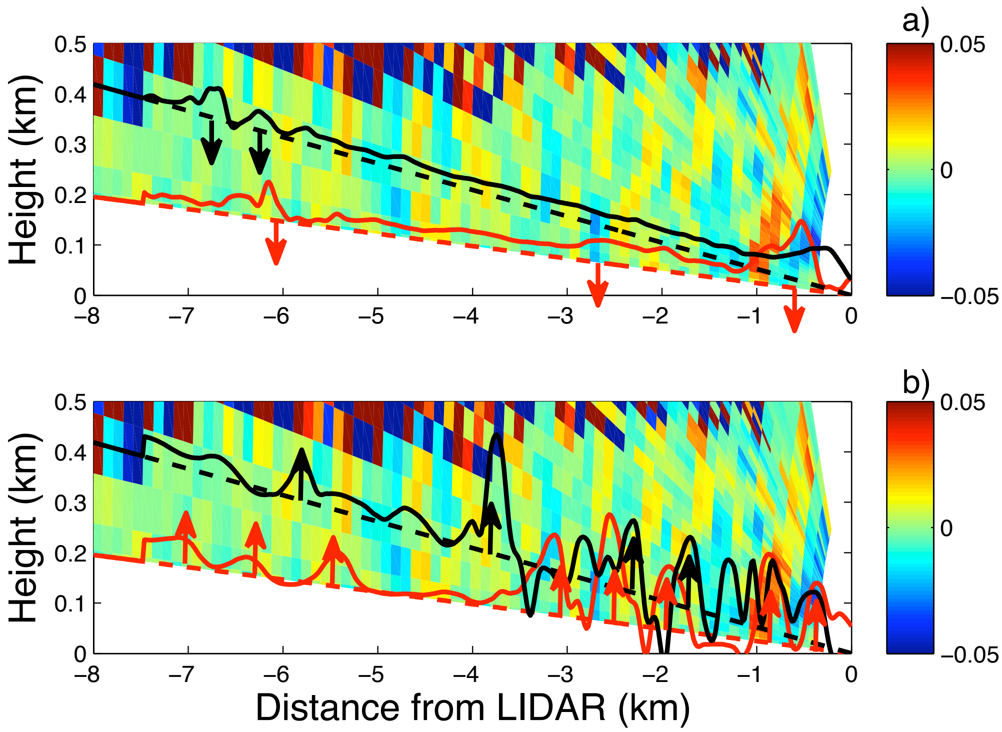

Fig. 3. Superposition of RHI scan and DLE fields. Color map is the radial gradient of the LOS velocity. a) Comparison with forward-time DLE. Peaks in DLE indicate downdrafts. b) Comparison with backward-time DLE. Peaks in DLE indicate updrafts. Note the correlation of various peaks and color contour maxima/minima.

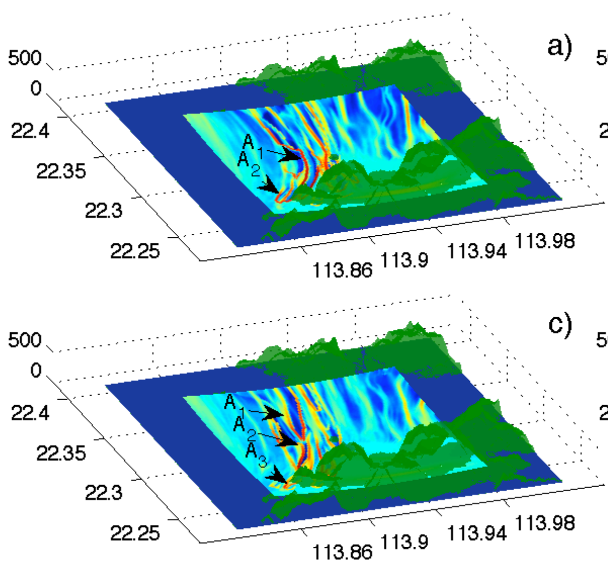

FIG. 4. Evolution of the hairpin structures at the Southwest corner of the domain. a) At 1417UTC, A_1 is detached from the mountain and A_2 start to emerge. b) At 1421UTC, as A_1 is advected away from the mountain peak, A_2 starts to grow. c) At 1425UTC, A_1 is advected further away and begin to decorrelate (vertical motion becomes weak, as inferred from the DIV field not shown here), A_2 saturates and about to detach from the peak. A_3 about to emerge as the flow move upward from the back of the peak. d) At 1429UTC, A_1 is about to leave the domain, A_2 detaches from the peak and A_3 starts to grow at the peak.

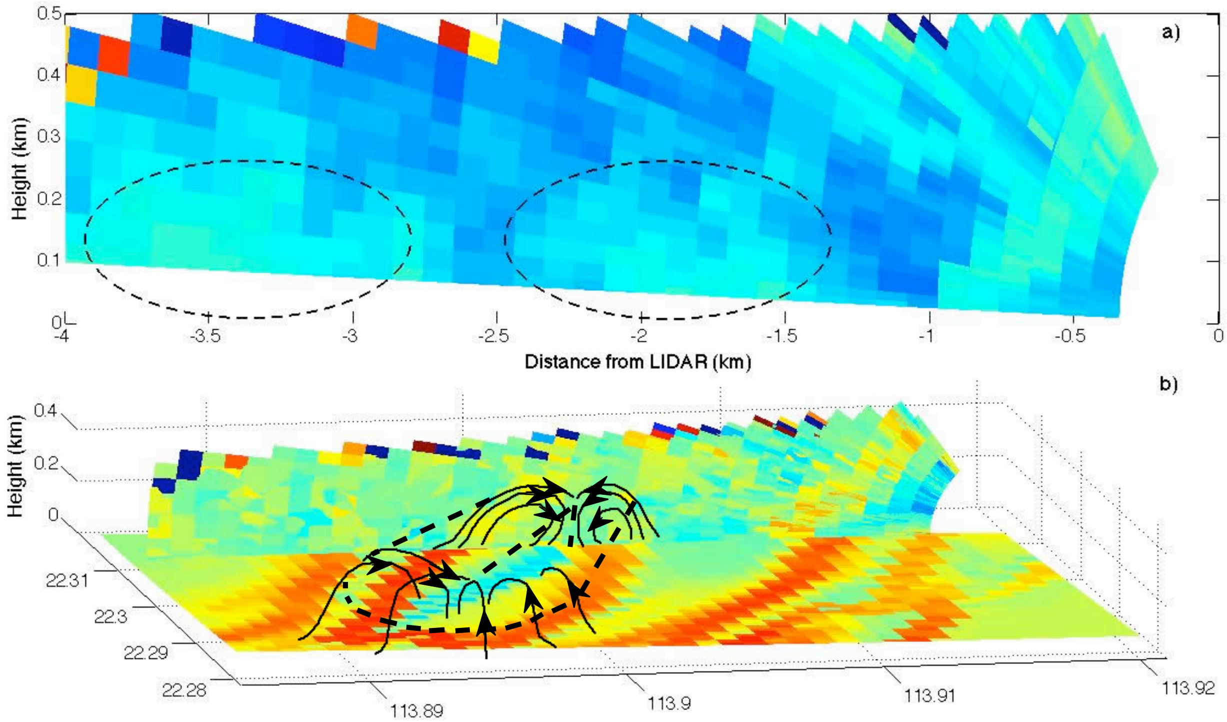

FIG. 5. Enlarged view from the South of the hairpin vortex A2. a) LOS velocity from the RHI scan. Vertical structures near ground are outlined with the dashed ellipses and have roughly a vertical length scale of 250 m. b) Flow structure and fluid trajectories inferred from the DLE field and RHI scan. Trajectories leave the conical scan plane by moving upward in the ridges of backward-time DLE. At about 250 m which is the top of near ground structures, they turn around and start to descend. Dashed curves outline the structure of the hairpin vortex.